# Quantum pumping through the surface states of a topological insulator

Hossein Nikoofard,[1,2] Mahdi Esmaeilzadeh,[1,*] Rouhollah Farghadan,[2] and Jia Tao Sun[3]
[1]*Department of Physics, Iran University of Science and Technology, Tehran 16844, Iran*
[2]*Department of Physics, University of Kashan, Kashan 87317-53153, Iran*
[3]*School of Information and Electronics, Beijing Institute of Technology, Beijing 100081, China*

(Received 5 February 2022; revised 8 August 2022; accepted 13 October 2022; published 25 October 2022)

We investigate quantum charge pumping through the surface states of a topological insulator (TI), i.e., $Bi_2Te_3$. We consider a device with two oscillating potentials for the generation of a dc current in the adiabatic pumping regime. Applying the exchange magnetic field, we show that the device can work as a memory read-out. Also, we show that by applying a static gate voltage the pumping device can work as a field-effect transistor. In addition, the pumped current obtained in our proposed device is significantly (more than three orders of magnitude) greater than the pumped current obtained previously for TI-based devices. These properties show that $Bi_2Te_3$ can be considered a good candidate for the fabrication of nanoelectronic devices based on TI as well as low-power and low-energy consumption devices in quantum computing.

DOI: 10.1103/PhysRevB.106.165127

## I. INTRODUCTION

Topological insulators (TIs) compared with conventional insulators, in addition to having bulk band gaps, are famous due to containing conductive states on their surface or edge [1,2]. The time-reversal symmetry and large spin-orbit interaction in TIs lead to spin-momentum locking and the appearance of the hexagonal warping (HW) effect in their surface states. At high Fermi energy, the shape of constant-energy contour related to surface states is changed from a circle to a snowflake due to the HW effect [3]. Also, TIs attract the attention of researchers as promising candidates for low-power and low-energy consumption electronic devices in quantum computing and as new materials for the fabrication of spintronic devices [3–8]. As a technical approach, resonant tunneling and switching effect have been investigated in field-effect transistors based on TIs [9]. Experimentally, an *n-p-n* junction of TIs has been introduced as a test sample for the study of the Hall effect [10].

Compounds based on Bi such as $Bi_2Te_3$ and $Bi_2Se_3$ have a single Dirac cone on their surface [11,12]. This feature opened the way for studying topological quantum computation and magnetotransport so some studies have been devoted to these materials from theoretical and experimental approaches [2,12–17]. Also, these compounds are well-known for the role of polarons on their thermal conductivity and applications in thermoelectric devices [18–22]. Moreover, the surface states in $Bi_2Se_3$ have been considered for the study of conductance and magnetoresistance in the presence of a periodic array of exchange magnetic fields [23]. The surface states of $Bi_2Se_3$ have been proposed as an optospintronic device with controllable spin polarization [24]. A high-performance magnetic field detector has been fabricated based on $Bi_2Te_3$ films [25]. A supercurrent is obtained through the surface states of $Bi_2Te_3$ in the Josephson junction as an experimental study [26]. Applying an in-plane magnetization on the surface states of $Bi_2Te_3$ can induce the quantum anomalous Hall effect [27]. Recently, electronic transport and magnetoresistance have been studied through the surface states of a double-gated $Bi_2Te_3$ [28]. The effect of quasiparticles on the band structure and transport properties of TI materials has been studied and shown that topological spin texture of surface states is preserved in the presence of chemical disorder [29,30]. The formation of charge puddles and their roles in transport have been investigated in compensated $Bi_2Te_3$ [31–33]. The introduction of disorder in $Bi_2Se_3$ causes the interplay between surface and bulk conductivities at different temperature [34].

In quantum pumping, dc current can be generated and modulated without using bias voltage [35]. An adiabatic quantum pumping regime is considered when the period of oscillating voltages is greater than the transmission time of charge carriers throughout the system. In the adiabatic regime of the quantum pumping method, only the electrons near the Fermi energy contribute to the generation of current, but in the nonadiabatic regime, other electrons also contribute in the generation of current [36]. In the adiabatic regime of the quantum pumping method, the dissipation for electron energy is about zero because this regime works near the equilibrium distribution of electron energies [37–40]. More studies have been devoted to the use of quantum pumping in nanoscale systems [41–52] and the significant impact of pumping in quantum computing [53,54]. The surface states of $Bi_2Se_3$ between two ferromagnetic layers are proposed for studying pumped current by using ferromagnetic resonance and time-resolved x-ray magnetic circular dichroism [1]. Experimentally, the pumped current is generated in a $Bi_2Se_3$ through magnetization dynamics of the metallic ferromagnet by applying an external rf-magnetic field [55]. Quantum

*mahdi@iust.ac.ir

 

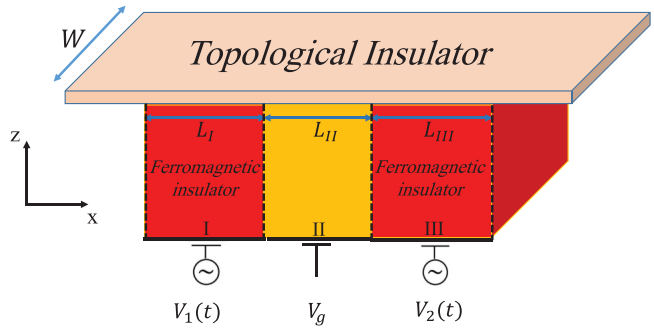


FIG. 1. Schematic view of a quantum pumping device based on $Bi_2Te_3$. For generating dc current, two oscillating potentials $V_1(t)$ and $V_2(t)$ are applied to regions I and III. Also, two exchange magnetic fields, induced by the proximity effect of ferromagnetic insulators, are applied in these regions. To control the pumped current, a static gate voltage $V_g$ is applied to region II. We also use an insulator in region II (shown in yellow) for excluding the permeate of the gate current.

pumping through the surface states of TI by applying two ac gate voltages or via rotation of exchange magnetic fields has been studied [56]. The main problem in the pumping method is its low current. For instance, the pumped current predicted for TI-based device is of picoampere order depending on parameters of the system [56]. However, in this work, we have achieved the nanoampere current for our TI-based proposed device.

In this work, we study quantum pumping through the surface states of $Bi_2Te_3$. The phase difference between two applied ac gate voltages causes the generation of pumped current. The dependence of pumped current on the direction of magnetization ($x$, $y$, and $z$) shows that the proposed device has a high sensitivity to magnetic configuration and it could be used as a magnetic device such as a memory read-out. Applying a static gate voltage, we can control the pumped current electrically which shows the proposed device can work as a TI-based field-effect transistor. Also, we take into account the influence of HW on the pumped current and show that ignoring this effect causes a significant overestimate of the pumped current. The pumped current obtained in our proposed device is more than three orders of magnitude greater than the maximum pumped current obtained previously for TI-based devices.

The rest of the paper is organized as follows. At first, we present system Hamiltonian and wave functions for surface states of $Bi_2Te_3$ and calculate the pumped current by using scattering matrix ($S$-matrix) method. Then numerical results of the pumped current and the influence of the exchange field and the static gate voltage are shown and discussed. Finally, a summary and conclusion are presented.

## II. MODEL AND HAMILTONIAN

We proposed a two-dimensional (2D) quantum pumping nanodevice based on the surface states of a topological insulator ($Bi_2Te_3$) as shown in Fig. 1. Tuning the Fermi level on the surface states via proper doping, we can avoid interaction between surface states with the bulk states [12]. To achieve the pumping current, two oscillating voltages as potential barriers are applied to regions I and III (see Fig. 1). Also, two exchange magnetic fields, induced by the proximity effect of the ferromagnetic insulator, are applied in these regions and a static gate voltage is applied in region II (central region) to control the charge current. The effective Hamiltonian of the system is given by [3,28]

$$\hat{H} = v_F(k_x\sigma_y - k_y\sigma_x) + \lambda\left(k_x^3 - 3k_xk_y^2\right)\sigma_z + eV\mathbf{I} + M\mathbf{a}\cdot\boldsymbol{\sigma}, \tag{1}$$

where the first term is the isotropic 2D Dirac fermion Hamiltonian and the second term is the HW effect with parameter $\lambda$ which is equivalent to the cubic Dresselhaus spin-orbit coupling in rhombohedral structures [3]. The last two terms indicate respectively the electric and exchange magnetic field applied to the system as perturbations. In Eq. (1), $\boldsymbol{\sigma} = (\sigma_x, \sigma_y, \sigma_z)$ are Pauli matrices, $k_x$ and $k_y$ are the $x$ and $y$ components of wave vector for incoming (outgoing) wave to (from) the barriers and $v_F$ is the Fermi velocity. In the third term, $-e$ is the electron charge, $V$ is the value of oscillating potentials or static gate, and $\mathbf{I}$ is the unit matrix. Also, in the last term, $\mathbf{a} = (\sin\theta\cos\phi, \sin\theta\sin\phi, \cos\theta)$ is the unit vector showing the direction of exchange magnetic field with normalized strength $M$. Here $\theta$ and $\phi$ are the polar angle concerning the $z$ axis and azimuthal angle concerning the $x$ axis, respectively. Diagonalizing the Hamiltonian, the eigenstates of the system for conduction and valence bands can be written as

$$E = eV \pm \sqrt{\left[\lambda\left(k_x^3 - 3k_xk_y^2\right) + M\cos\theta\right]^2 + A}, \tag{2}$$

where

$$A = (M\sin\theta\cos\phi - v_Fk_y)^2 + (M\sin\theta\sin\phi + v_Fk_x)^2, \tag{3}$$

and sign $+(-)$ in Eq. (2) denotes the conduction (valence) band.

In a pumping device shown in Fig. 1, the dc current is generated due to the breaking of both time-reversal and spatial symmetries via modulation of oscillating potentials that are supposed as $V_1(t) = V_{01} + \delta V_1\sin(\omega t)$ and $V_2(t) = V_{02} + \delta V_2\sin(\omega t + \varphi)$. Here $V_{01}$ and $V_{02}$ are the static part of potentials, $\delta V_1$ and $\delta V_2$ are the ac amplitudes, $\omega$ is the frequency of oscillations, and $\varphi$ is the phase difference between left and right oscillating potentials. There are three regions $j =$ I, II, and III, which are separated with boundaries indicated by dashed lines in Fig. 1. One can consider electrons incident to the system with angle $\alpha$ with respect to $x$ axis and use $k_y = k_x\tan\alpha$. So, for a given value of $E$, i.e., $E = E_F$, and a given value of $\alpha$, Eq. (2) can be written as a six-order equation in terms of $k_x$ as follows:

$$\begin{aligned}&\lambda^2(3\tan^2\alpha - 1)^2{k_x}^6 - 2\lambda M\cos\theta(3\tan^2\alpha - 1){k_x}^3\\ &+ {v_F}^2(1 + \tan^2\alpha){k_x}^2 + 2v_FM\sin\theta(\sin\phi - \cos\phi\tan\alpha)k_x\\ &+ M^2 - (E - eV)^2 = 0.\end{aligned} \tag{4}$$

Solving the above equation, six roots are obtained as $k_{x,n}$ where $n = 1, \ldots, 6$. In $S$-matrix method, the $S$ matrix of each region can be calculated by considering each region as a separate scatterer or barrier with zero external fields ($M = V = 0$) in its left and right sides [57,58]. The whole system $S$ matrix can be obtained using the individual $S$ matrix of all regions.

The wave functions of Hamiltonian in Eq. (1) for the inside of region $j$ and its left and right sides can be written as [28]

$$\Psi_L(\mathbf{k}) = \psi\left(k_x^{(i)}, k_y\right) + \sum_{n=1}^{3} r_n \psi\left(k_{x,n}^{(r)}, k_y\right), \quad x < x_{1j}, \tag{5}$$

$$\Psi_C(\mathbf{k}) = \sum_{n=1}^{6} f_n \psi\left(k_{x,n}^{(c)}, k_y\right), \quad x_{1j} < x < x_{2j}, \tag{6}$$

$$\Psi_R(\mathbf{k}) = \sum_{n=1}^{3} t_n \psi\left(k_{x,n}^{(t)}, k_y\right), \quad x > x_{2j}, \tag{7}$$

where

$$\psi(k_{x,n}, k_y) = \sqrt{\frac{|B_{1n}|^2}{|B_{1n}|^2 + |B_{2n}|^2}} \begin{pmatrix} 1 \\ \frac{B_{2n}}{B_{1n}} \end{pmatrix} e^{ik_{x,n}x} e^{ik_y y}, \tag{8}$$

$$B_{1n}(k_{x,n}, k_y) = M\cos\theta + (E - eV) + \lambda k_{x,n}\left(k_{x,n}^2 - 3k_y^2\right), \tag{9}$$

and

$$B_{2n}(k_{x,n}, k_y) = M\sin\theta e^{i\phi} - v_F(k_y - ik_{x,n}). \tag{10}$$

In the above equations, indices $L$, $R$ and $C$ refer to left, right and inside of region $j$, $r_n$ and $t_n$ are respectively the reflection and transmission coefficients for root $n$, and $f_n$ is the scattering amplitude. Using Eq. (5)–(7) and applying the boundary conditions at $x_{1j}$ and $x_{2j}$ for wave function and its first and second derivatives, one can obtain $r_n$, $t_n$, and $f_n$ [49]. Also, $k_x^{(i)}$, $k_{x,n}^{(r)}$, and $k_{x,n}^{(t)}$ are respectively the incident, reflected, and transmitted wave vectors of electrons for left and right sides of a region. $k_x^{(c)}$ is the $x$ component of the wave vector inside of a region. As the first set of solutions related to Eq. (4), if $E < E_{\rm cr}$, where $E_{\rm cr} \approx 377$ meV is a critical Fermi energy of $Bi_2Te_3$ [59], two roots of $k_x$ are real and four ones are imaginary. For $E > E_{\rm cr}$, as a second set of solutions, six roots are real [59,60].

Now for first set of solutions, we select $k_x^{(i)} = k_{x,1}^{(t)} = -k_{x,1}^{(r)}$ as a real positive root and $k_{x,2}^{(t)} = -k_{x,2}^{(r)}$ and $k_{x,3}^{(t)} = -k_{x,3}^{(r)}$ as two complex roots with positive imaginary part [59]. We select the $r_1$ and $t_1$ which indicate the propagation modes related to $k_{x,1}$. The $S$ matrix for each region can be defined as $S_j = [(r_j, t_j)^T (t_j', r_j')^T]$ where the superscript $T$ stands for transpose, $r_j'$ and $t_j'$ are reflection and transmission coefficients for incident electrons from right side of the region $j$, respectively [57]. To calculate the reflection and transmission coefficients, we have imposed wave-function matching conditions at all interfaces of Fig. 1.

For second set of solutions, one can select $k_x^{(i)} = k_{x,1}^{(t)} = -k_{x,1}^{(r)}$, $k_{x,2}^{(t)} = -k_{x,2}^{(r)}$, and $k_{x,3}^{(t)} = -k_{x,3}^{(r)}$ so that group velocity of electron along $x$ direction for $k_{x,1}^{(t)}$, $k_{x,2}^{(t)}$, and $k_{x,3}^{(t)}$ must be positive. In this case, the $S$ matrix is a $6\times6$ matrix and the reflection and transmission coefficients are $3\times3$ matrices [59]. The $S$ matrix for whole system, as mentioned before, is given by using individual $S$ matrix of all region, i.e., $S = S_{\rm I} \otimes S_{\rm II} \otimes S_{\rm III}$ (see Ref. [57] and Appendix B of Ref. [49]). Using whole system $S$ matrix, the pumped current for a quantum state $k$ is given by [51,61]

$$I_k = \frac{\omega e(\sin\varphi)\delta V_1 \delta V_2}{2\pi} \sum_{\beta} \sum_{\beta'} \mathrm{Im}\left(\frac{\partial (S_{\beta\beta'})^*}{\partial V_1} \frac{\partial S_{\beta\beta'}}{\partial V_2}\right), \tag{11}$$

where index $\beta'$ refers to the incoming modes to the channel from the left and right sides and $\beta$ refers to outgoing modes from the left side [62]. In weak pumping regime (i.e., $V_0 \gg \delta V$) the derivations $\frac{\partial S}{\partial V_i}$ are independent of time [61]. To consider all of the quantum states for a given Fermi energy, the summation over $k$ is needed. Using $k_x = k\cos\alpha$ and $k_y = k\sin\alpha$, the summation over $k$ can be converted to an integral over angle $\alpha$ and the total pumped current can be written as (see Appendix for more details)

$$I = \sum_k I_k = \frac{W}{2\pi} \int_{-k_y^{\max}}^{+k_y^{\max}} I_k(k_y) dk_y = \frac{W}{2\pi} \int_{-\frac{\pi}{2}}^{\frac{\pi}{2}} I_\alpha(\alpha) F(\alpha) d\alpha, \tag{12}$$

where $F(\alpha)$ is defined in Eq. (A2) of Appendix.

## III. RESULTS AND DISCUSSION

For numerical study, we consider the surface of $Bi_2Te_3$ with width $W = 10$ $\mu$m [46,62] which two oscillating potentials and two exchange magnetic fields are applied in regions I and III as shown in Fig. 1. We also consider the static part of oscillating potentials as $eV_{01} = eV_{02} = 350$ meV [28], their ac amplitude as $e\delta V_1 = e\delta V_2 = 0.2$ meV [62] and their oscillation frequency as $\omega = 5$ GHz [56,62]. The phase difference between left and right potential barriers is selected as $\varphi = \pi/2$ to have maximum dc pumped current [see Eq. (11)]. To control pumped current, an external static gate voltage ($V_g$) is also applied in region II (see Fig. 1). The lengths of the three regions are considered as $L_I = L_{\rm II} = L_{\rm III} = 20$ nm [56,62]. The HW parameter and normalized Fermi velocity for $Bi_2Te_3$ are reported as $\lambda = 250$ meV nm$^3$ and $v_F = 255$ meV nm, respectively [3]. We also consider the exchange magnetic fields in the parallel configuration with normalized strength $M = 80$ meV [28,56,63] except in Fig. 3.

The electron energy contours corresponding to the Dirac cone are shown in Fig. 2. In Fig. 2(a), the energy contours are sketched in the absence of any applied external perturbations such as oscillating potential and exchange magnetic field. It is observed that for the high values of energy, the contours deform from circle to snowflake due to the HW effect. We will show this effect in more detail later (see Fig. 6). With applying a gate potential barrier with $eV_0 = 350$ meV [see Fig. 2(b)], area of contour becomes smaller [compare Figs. 2(a) and 2(b)]. This is because the conduction and valence bands move upward due to the presence of potential and electron Fermi energy cuts the valence band in the lower cross-section. Note that, as shown in Figs. 2(a) and 2(b), for the conduction (valence) band, energy increases (decreases) from the central contours to the outer ones. In Fig. 2(c), in addition to gate potential, an exchange magnetic field is applied in the $x$ direction. The exchange field moves the Dirac point $\Gamma$ in the $k_y$ direction and mirror symmetry is broken in the $x$ direction. In the same case (not shown here) if the magnetization is applied

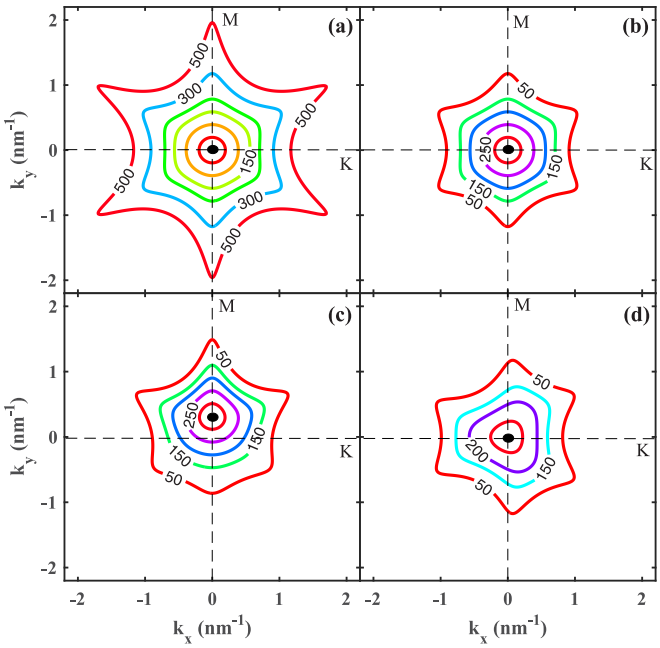


FIG. 2. Energy contours corresponding to Dirac cone for several values of energy when the symmetric points of the system are shown with Γ (black circle), $M$ and $K$, (a) in the absence of any external perturbations, (b) in the presence of gate potential with $eV_0 = 350$ meV, (c) in the presence of both gate potential and exchange magnetic field applied in the $x$ direction, and (d) similar to (c) but the exchange field is applied in the $z$ direction.

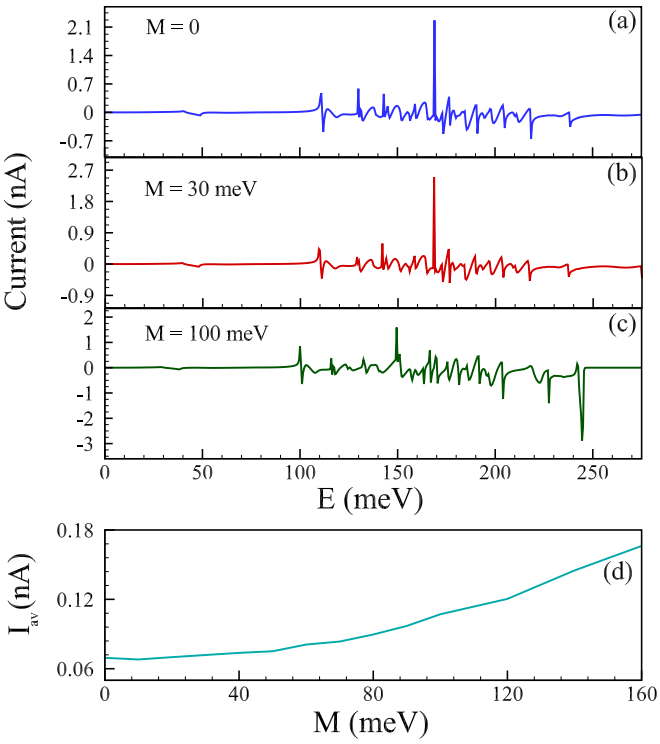


FIG. 3. [(a)–(c)] Pumped current versus the Fermi energy $E$ for different values of exchange magnetic field applied along the $z$ direction. (d) Average pumped current versus the exchange magnetic field.

in the $y$ direction, Γ point moves in the $k_x$ direction, and mirror symmetry is broken in the $y$ direction. If the direction of magnetization is fixed along the $z$ direction as shown in Fig. 2(d), the contour plot modifies and the mirror symmetries are broken in both $x$ and $y$ directions. Also, in this case, the Dirac cone shifts along the $z$ axis (not shown in the figure).

In Fig. 3, the pumped current is shown for different values of exchange magnetic field applied along the $z$ direction. A comparison between the pumped currents in the absence of exchange magnetic field [see Fig. 3(a)] and in the presence of this field [see Figs. 3(b) and 3(c)] shows that the presence of an exchange magnetic field does not induce magnetoresistance but, in contrast, it causes an increase in the pumped current. To clearly show this effect, let us define the average of current absolute value as

$$I_{\rm av} = \frac{1}{E_{\rm fin} - E_{\rm ini}} \int_{E_{\rm ini}}^{E_{\rm fin}} |I| dE, \tag{13}$$

where $E_{\rm ini}$ and $E_{\rm fin}$ are respectively the initial and final values of energy chosen for integration. Here $E_{\rm ini} = 0$ and $E_{\rm fin}$ is equal to a value after that the pumped current becomes almost zero. In our calculations, we chose $E_{\rm fin} = 350$ meV. Figure 3(d) shows the average pumped current $I_{\rm av}$ versus the exchange magnetic field $M$. It is observed that with increasing exchange magnetic field, average pumped current increases which is in agreement with previous studies (see e.g., Refs. [64,65]). The main feature of our proposed device based on $Bi_2Te_3$ is the magnitude of its pumped current. The pumped current, as shown in Fig. 3, is of nanoampere order which is several orders of magnitude greater than the pumped current obtained previously for TI-based devices. For example, the pumped current obtained in Ref. [56] is of picoampere order. As shown in Figs. 3(a)–3(c), the pumped current exhibits fast fluctuations with changing Fermi energy. These fluctuations increase (decrease) by increasing (decreasing) the length of oscillating potentials (i.e., $L_I$ and $L_{\rm III}$) [51], and thus one can manipulate these fluctuations by changing $L_I$ and $L_{\rm III}$. Another factor that affects the oscillations of the pumped current is the distance between two oscillating potentials (i.e., $L_{\rm II}$) [58]. The fluctuations arising from this distance are related to the Fabry-Perot resonances formed by the interference of waves reflected between the two oscillating potentials [66].

To study the effect of exchange magnetic field more precisely, we plot the pumped current in Fig. 4 for various directions of magnetization by considering a small interval of Fermi energy (i.e., $E = 133.5$–$141$ meV). As shown in Fig. 4(a), one can control the pumped current magnetically through the rotation of the direction of the exchange magnetic field. For example, the points indicated by the black circle show the values of Fermi energy in which the pumped current becomes zero when the magnetization is fixed along one axis but for two other magnetization directions, the pumped current has a nonzero value. In Fig. 4(b), we plot the pumped current versus Fermi energy for one (left) exchange field along $+x$ and $-x$ directions, while the other (right) exchange field is kept fixed along $+x$. As we see in this figure, the pumped current has different values for $+x$ and $-x$ directions. Thus the device can discriminate between $+x$ and $-x$ directions and can be considered as a memory read-out [63]. Also, it is observed that the pumped current is smaller for $-x$ direction.

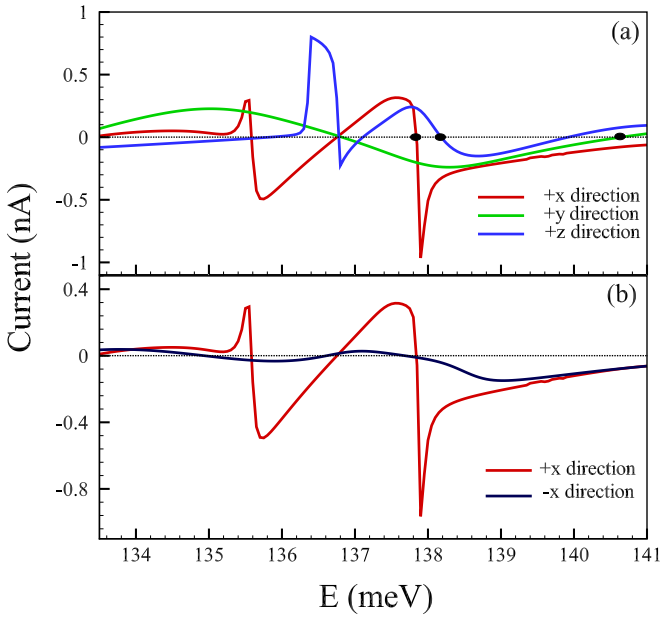


FIG. 4. Pumped current versus the Fermi energy $E$ (a) for $x$, $y$, and $z$ directions of exchange magnetic fields and (b) for $+x$ and $-x$ directions of the first (left) exchange magnetic field. Here the second (right) exchange field is kept fixed along $+x$ direction. The zero line is indicated by a black dotted line.

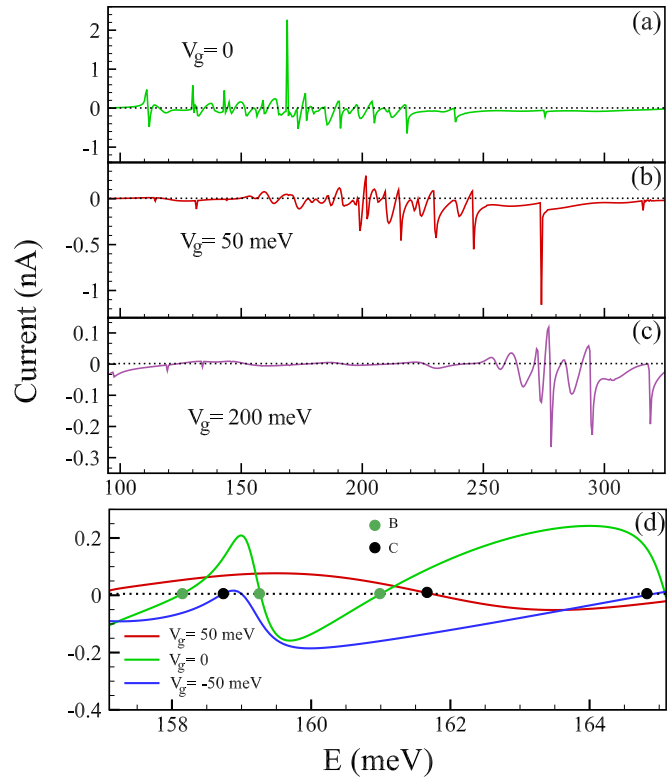


FIG. 5. [(a)–(c)] Pumped current versus the Fermi energy $E$ for three values of the static gate in the absence of the exchange magnetic field. (d) Pumped current in a small interval of Fermi energy (i.e., $E = 157.1$–$165.1$ meV) for $V_g = -50,\ 0,$ and 50 meV. The black dotted lines indicate the zero lines.

This is due to this fact that for $-x$ direction, two exchange fields are antiparallel which causes a decrease in pumped current [49,67].

We now study the effect of a static gate voltage applied on the central region of the device (region II of Fig. 1) and plot the pumped current for three values of static gate voltage in Fig. 5. As shown in Figs. 5(a)–5(c), by increasing the static gate voltage the value of the pumped current decreases. The decrease of pumped current in the presence of gate potential is due to the decrease of cross-section of energy contours (see Fig. 2) and thus the decrease in the number of transport channels. Also, the gate voltage acts as a potential barrier, and one can change and control the pumped current by changing the static gate voltage. Hence as an interesting result, the proposed pumping device can work as a field-effect transistor [68]. Figure 5(d) shows the effect of gate voltage in a small interval of Fermi energy (i.e., $E = 157.1$–$165.1$ meV). In this figure, the points indicated by $B$ show the values of Fermi energy at which the pumped current is zero in the absence of gate voltage, and by turning on the gate voltage, the pumped current becomes nonzero. Also, in these points, changing the sign of gate voltage, the direction of the pumped current is reversed. Inversely, at the points indicated by $C$, by turning on a positive or negative gate voltage, the pumped current becomes zero. At both points $B$ and $C$, the gate voltage acts as a switch for pumped current.

Now, we study the effect of HW on pumped current and we plot the current versus the Fermi energy in Fig. 6 for both taking into account [$\lambda = 250$ meV nm$^3$] and ignoring ($\lambda = 0$) the HW effect. A comparison between Figs. 6(a) and 6(b) shows that by taking into account the HW effect the pumped current is significantly smaller than the current when the HW effect is ignored. Hence ignoring this effect causes an overestimate of pumped current. This is due to the fact that the HW effect causes the cross-section of the energy contours to become smaller [as shown in the right panel of Figs. 6(a) and 6(b)] and as a result, the number of transport channels decreases which causes a decrease in pumped current. Also, the circular contours deform and some of them become snowflakes due to the HW effect [see right panels of Figs. 6(a) and 6(b)]. The snowflake shape of the spin texture causes another decrease in the pumped current. To show the HW effect exclusively on spin texture, in Fig 6(c) the pumped current is depicted when the density of carriers is kept constant by changing the potential gates. A comparison between Figs. 6(b) and 6(c) indicates that except of the largest peak of Fig. 6(c), the decreases of pumped currents due to the HW effect are almost the same for both figures which shows that the effect of HW on spin texture is greater than its effect on carrier density. The effect of HW has been already discussed in conventional (nonpumping) electron transport [69–71], but in the previous studies of quantum pumping in TIs, this effect has been ignored [1,55,56,72].

Thus far, we made the assumption that the exchange magnetic field directions are aligned, but this assumption is difficult in practice. We now investigate the effect of the misalignment of exchange field directions on the pumped current and the result is shown in Fig. 7. This figure shows the pumped currents for misalignments about 5% and 10%. The pumped

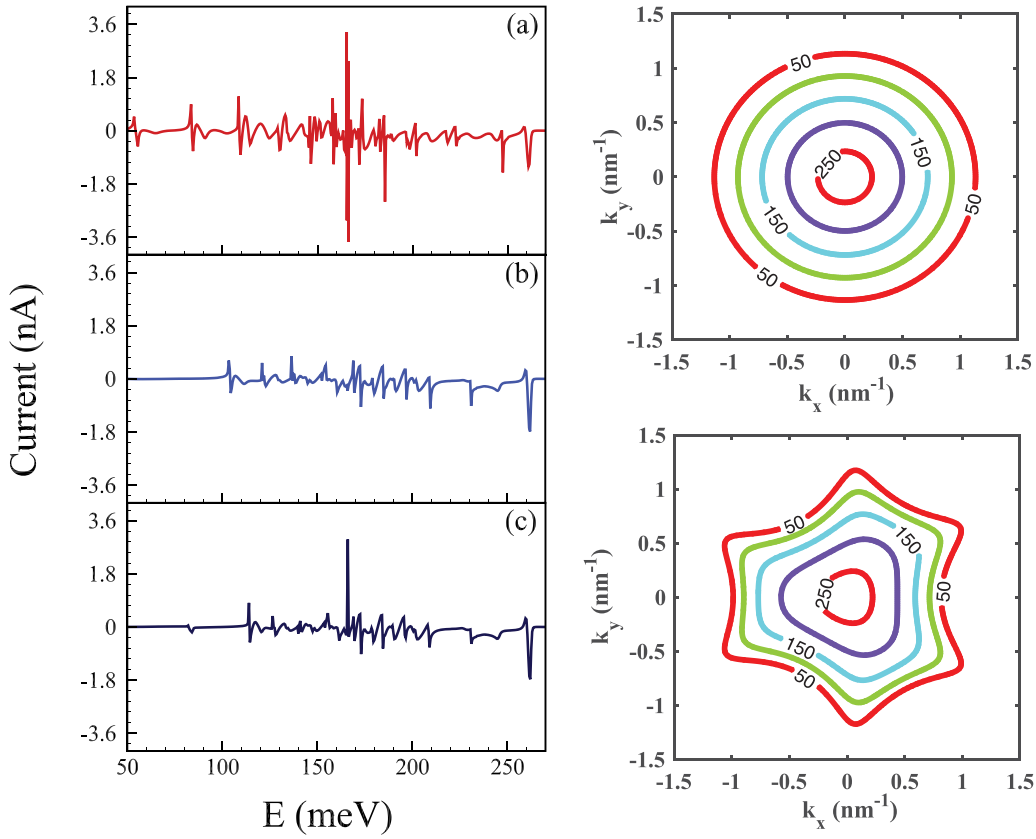


FIG. 6. (Left) Pumped current versus the Fermi energy $E$ for (a) in the absence of HW ($\lambda = 0$) and (b) and (c) in the presence of HW ($\lambda = 250$ meV nm$^3$) when the exchange magnetic field is applied in the $z$ direction and the static gate voltage is absent. In (b), the total effects of HW on carriers density and spin texture are considered, while in (c), only the effect of HW on the spin texture is considered. (Right) Energy contours of valence band corresponding to (a) and (b) on the left, respectively.

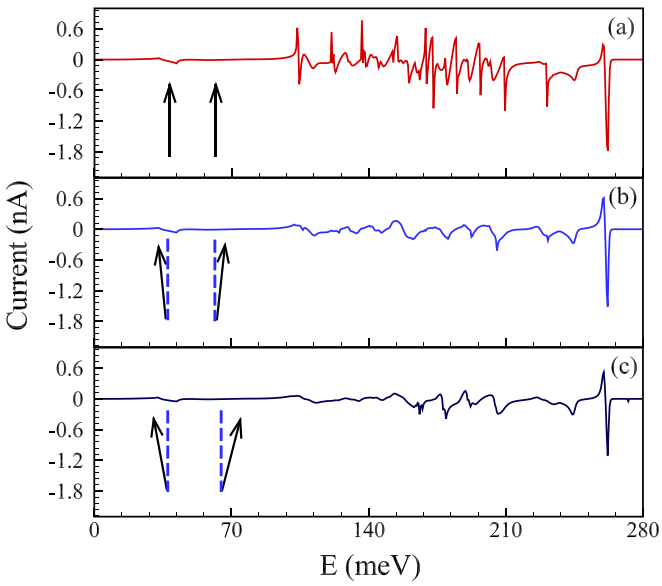


FIG. 7. Pumped current versus the Fermi energy $E$ for (a) exchange fields are aligned ($\theta_1 = \theta_2 = 0$), (b) exchange fields with about 5% misalignment ($\theta_1 = 5^\circ$, $\phi_1 = 0$ and $\theta_2 = 5^\circ$, $\phi_2 = 180^\circ$), and (c) exchange fields with about 10% misalignment ($\theta_1 = 8^\circ$, $\phi_1 = 0$ and $\theta_2 = 10^\circ$, $\phi_2 = 180^\circ$).

current for the case in which the fields are aligned is shown in this figure for comparison. It is observed that misalignment cause to decrease in the value and fluctuations rate of pumped current but it does not destroy the pumping effect.

As shown in Figs. 3–7, the pumped current is very sensitive to the Fermi energy $E$. It is worth to mention that, in practice, the Fermi energy $E$ can be changed and controlled sufficiently well by using a back gate (see e.g., Ref. [73]). The relation between the Fermi energy and gate voltage depends on some parameters such as dielectric constant and thickness of substrate [74]. Using a digital-to-analog converter (DAC) [75] with at least 16 bits and choosing appropriate parameters (with dielectric constant 2900 and thickness 0.1 $\mu$m), one can control the gate voltage with step 0.075 mV and thus the Fermi energy with small step 0.05 meV in energy interval 0 to 300 meV which has been used in our calculations (see Figs. 3–7).

Quasiparticles in the bulk of TI materials, which may be due to the disorder effects and charge puddles, could affect the surface state transport properties in TI materials [76,77]. As mentioned in Sec. II, by tuning the Fermi level in TI materials via proper doping, one can decrease the interaction between the bulk states and surface states [78,79]. Doping of impurities (such as Sb) in bulk, tuning the gate voltage and fabrication of ultrathin TI films are effective methods to

reduce the bulk effects on surface transport [80–82]. The doping causes the surface mobility becomes 12 times greater than the bulk mobility [83]. Using gate voltage causes to increase the bulk resistivity 4 times and decrease the bulk mobility by two orders of magnitude [84,85]. Also, the decoupling of surface state conductance and bulk state conductance was reported in a TI ($(Bi_2Te_2Se)$ in temperatures below 10 K [86]. By adding vacancy to $Bi_2Te_3$, surface mobility at temperatures below 10 K is about 60 times greater than bulk mobility, and therefore the bulk states effects on transport could be ignored with a good approximation [87]. Controlling the charge puddle formation via temperature is suggested for the reduction of bulk effects in transport in TI materials [88]. Compensation of intrinsic charges via low-temperature (4–10 K) electron irradiation is another method for decreasing the effects of bulk states on TIs transport [31].

## IV. SUMMARY AND CONCLUSION

In summary, we have studied quantum pumping transport properties in the surface states of a topological insulator ($Bi_2Te_3$) using the $S$-matrix approach. Applying two oscillating potentials with a phase difference, a dc current can be generated in the system without using bias voltage. We have investigated the effect of the exchange magnetic field, induced by the ferromagnetic insulator, on the pumped current and shown that by changing the magnetization direction the pumped current can be controlled and the device can be used as a TI-based memory read-out. Also, we have shown that one can control the pumped current electrically by applying a static gate voltage and the device can work as a field-effect transistor. The memory read-out and field effect transistor devices proposed in the present study are based on the surface states of a topological insulator and thus are two-dimensional. They have some advantages relative to conventional (three-dimensional) devices such as low dimensions, small sizes, and extremely low power consumption. Moreover, we have taken into account the HW effect in Hamiltonian and we have shown that ignoring this effect leads to an overestimate of the pumped current. The results of this study show that $Bi_2Te_3$ can be considered as a promising candidate for the fabrication of nanoelectronic devices based on TI.

## ACKNOWLEDGMENT

This work was supported by the Iran National Science Foundation (INSF) under Grant No. 97007576.

## APPENDIX

In the following, we show the method for changing the integral variable, in Eq. (12), from $k_y$ to $\alpha$. We know $k_y = k\sin\alpha$, so we define $F(\alpha)$ as follows:

$$dk_y = F(\alpha)d\alpha, \tag{A1}$$

where

$$F(\alpha) = \sin\alpha\frac{\partial k}{\partial\alpha} + k\cos\alpha. \tag{A2}$$

For determination of $\partial k/\partial\alpha$, it is necessary to know a relation between $k$ and $\alpha$. Using Eq. (2) for $V = M = 0$ then we have

$$E = \sqrt{(\lambda k^3\cos 3\alpha)^2 + (v_F k)^2}. \tag{A3}$$

With solving above equation for $E = E_F$

$$k = \sqrt{\sqrt[3]{\sqrt{Q^3+R^2}+R} - \sqrt[3]{\sqrt{Q^3+R^2}-R}}, \tag{A4}$$

where

$$Q = \frac{v_F^2}{3\lambda^2\cos^2 3\alpha},$$
$$R = \frac{E_F^2}{\lambda^2\cos^2 3\alpha}, \tag{A5}$$

and

$$\frac{\partial k}{\partial\alpha} = \frac{\sin 6\alpha}{4k\cos^2 3\alpha}\left[\left(\frac{3Q^3+R^2}{\sqrt{Q^3+R^2}}+R\right)(\sqrt{Q^3+R^2}+R)^{-2/3} - \left(\frac{3Q^3+R^2}{\sqrt{Q^3+R^2}}-R\right)(\sqrt{Q^3+R^2}-R)^{-2/3}\right]. \tag{A6}$$

[1] A. A. Baker, A. I. Figueroa, L. J. Collins-McIntyre, G. Van Der Laan, and T. Hesjedal, Spin pumping in ferromagnet-topological insulator-ferromagnet heterostructures, Sci. Rep. **5**, 7907 (2015).

[2] H. Zhang, C.-X. Liu, X.-L. Qi, X. Dai, Z. Fang, and S.-C. Zhang, Topological insulators in $Bi_2Se_3$, $Bi_2Te_3$ and $Sb_2Te_3$ with a single Dirac cone on the surface, Nat. Phys. **5**, 438 (2009).

[3] L. Fu, Hexagonal Warping Effects in the Surface States of the Topological Insulator $Bi_2Te_3$, Phys. Rev. Lett. **103**, 266801 (2009).

[4] A. Navabi, Y. Liu, P. Upadhyaya, K. Murata, F. Ebrahimi, G. Yu, B. Ma, Y. Rao, M. Yazdani, M. Montazeri, L. Pan *et al.*, Control of Spin-Wave Damping in YIG Using Spin Currents from Topological Insulators, Phys. Rev. Appl. **11**, 034046 (2019).

[5] H.-M. Guo and M. Franz, Theory of quasiparticle interference on the surface of a strong topological insulator, Phys. Rev. B **81**, 041102(R) (2010).

[6] X. Zhou, C. Fang, W.-F. Tsai, and J. Hu, Theory of quasiparticle scattering in a two-dimensional system of helical Dirac fermions: Surface band structure of a three-dimensional topological insulator, Phys. Rev. B **80**, 245317 (2009).

[7] Y. Tokura, K. Yasuda, and A. Tsukazaki, Magnetic topological insulators, Nat. Rev. Phys. **1**, 126 (2019).

[8] D. Pesin and A. H. MacDonald, Spintronics and pseudospintronics in graphene and topological insulators, Nat. Mater. **11**, 409 (2012).

[9] M. Vali, D. Dideban, and N. Moezi, Quantum well resonant tunneling FET based on topological insulator, Superlattices Microstruct. **100**, 1256 (2016).

[10] A. Banerjee, A. Sundaresh, S. Biswas, R. Ganesan, D. Sen, and P. S. Anil Kumar, Quantized transport in topological insulator n-p-n junctions, arXiv:1803.11367.

[11] Y. Xia, D. Qian, D. Hsieh, L. Wray, A. Pal, H. Lin, A. Bansil, D. Grauer, Y. S. Hor, R. J. Cava *et al.*, Observation of a large-gap topological-insulator class with a single Dirac cone on the surface, Nat. Phys. **5**, 398 (2009).

[12] Y. L. Chen, J. G. Analytis, J. H. Chu, Z. K. Liu, S. K. Mo, X. L. Qi, H. J. Zhang, D. H. Lu, X. Dai, Z. Fang *et al.*, Experimental realization of a three-dimensional topological insulator, $Bi_2Te_3$, Science **325**, 178 (2009).

[13] L. Fu and C. L. Kane, Superconducting Proximity Effect and Majorana Fermions at the Surface of a Topological Insulator, Phys. Rev. Lett. **100**, 096407 (2008); Topological insulators with inversion symmetry, Phys. Rev. B **76**, 045302 (2007).

[14] D. Hsieh, D. Qian, L. Wray, Y. Xia, Y. S. Hor, R. J. Cava, and M. Z. Hasan, A topological Dirac insulator in a quantum spin Hall phase, Nature (London) **452**, 970 (2008).

[15] D. Hsieh, Y. Xia, L. Wray, D. Qian, A. Pal, J. H. Dil, J. Osterwalder, F. Meier, G. Bihlmayer, C. L. Kane *et al.*, Observation of unconventional quantum spin textures in topological insulators, Science **323**, 919 (2009).

[16] G. M. Stephen, O. A. Vail, J. E. DeMell, A. T. Hanbicki, P. J. Taylor, and A. L. Friedman, Nonlocal Measurement as a Probe of the Spin Hall Effect in Topological Insulators, Phys. Rev. Appl. **16**, 034007 (2021).

[17] G. Kunakova, T. Bauch, X. Palermo, M. Salvato, J. Andzane, D. Erts, and F. Lombardi, High-Mobility Ambipolar Magnetotransport in Topological Insulator $Bi_2Se_3$ Nanoribbons, Phys. Rev. Appl. **16**, 024038 (2021).

[18] P. Larson, V. A. Greanya, W. C. Tonjes, R. Liu, S. D. Mahanti, and C. G. Olson, Electronic structure of $Bi_2X_3$(S, Se, T) compounds:Comparison of theoretical calculations with photoemission studies, Phys. Rev. B **65**, 085108 (2002).

[19] G. S. Hegde, A. N. Prabhu, R. Y. Huang, and Y. K. Kuo, Reduction in thermal conductivity and electrical resistivity of indium and tellurium co-doped bismuth selenide thermoelectric system, J. Mater. Sci.: Mater. Electron. **31**, 19511 (2020).

[20] G. S. Hegde, A. N. Prabhu, and M. K. Chattopadhyay, Improved electrical conductivity and power factor in Sn and Se co-doped melt-grown $Bi_2Te_3$ single crystal, J. Mater. Sci.: Mater. Electron. **32**, 24871 (2021).

[21] G. S. Hegde, A. N. Prabhu, A. Rao, and P. D. Babub, Enhancement of thermoelectric performance of In doped $Bi_2Te_{2.7}Se_{0.3}$ compounds, Phys. B: Condens. Matter **584**, 412087 (2020).

[22] V. Rathore, R. C. Dixit, R. R. Kinge, and K. K. Choudhary, Analysis of size dependent electrical resistivity of $Bi_2Te_3$ nanoparticles, AIP Conf. Proc. **2369**, 020225 (2021).

[23] Y. Zhang and F. Zhai, Tunneling magnetoresistance on the surface of a topological insulator with periodic magnetic modulations, Appl. Phys. Lett. **96**, 172109 (2010).

[24] Z.-H. Zhu, C. N. Veenstra, S. Zhdanovich, M. P. Schneider, T. Okuda, K. Miyamoto, S.-Y. Zhu, H. Namatame, M. Taniguchi, M. W. Haverkort *et al.*, Photoelectron Spin-Polarization Control in the Topological Insulator $Bi_2Se_3$, Phys. Rev. Lett. **112**, 076802 (2014).

[25] H. B. Zhang, H. Li, J. M. Shao, S. W. Li, D. H. Bao, and G. W. Yang, High-performance $Bi_2Te_3$-based topological insulator film magnetic field detector, ACS Appl. Mater. Interfaces **5**, 11503 (2013).

[26] M. Veldhorst, M. Snelder, M. Hoek, T. Gang, V. K. Guduru, X. L. Wang, U. Zeitler, W. G. Van Der Wiel, A. A. Golubov, H. Hilgenkamp *et al.*, Josephson supercurrent through a topological insulator surface state, Nat. Mater. **11**, 417 (2012).

[27] X. Liu, H.-C. Hsu, and C.-X. Liu, In-Plane Magnetization-Induced Quantum Anomalous Hall Effect, Phys. Rev. Lett. **111**, 086802 (2013).

[28] M. Arabikhah and A. Saffarzadeh, Surface state transport in double-gated and magnetized topological insulators with hexagonal warping effects, J. Phys.: Condens. Matter **31**, 445001 (2019).

[29] O. V. Yazyev, E. Kioupakis, J. E. Moore, and S. G. Louie, Quasiparticle effects in the bulk and surface-state bands of $Bi_2Se_3$ and $Bi_2Te_3$ topological insulators, Phys. Rev. B **85**, 161101(R) (2012).

[30] M. C. Martínez-Velarte, B. Kretz, M. Moro-Lagares, M. H. Aguirre, T. M. Riedemann, T. A. Lograsso, L. Morellon, M. R. Ibarra, A. Garcia-Lekue, and D. Serrate, Chemical disorder in topological insulators: A route to magnetism tolerant topological surface states, Nano Lett. **17**, 4047 (2017).

[31] C. W. Rischau, A. Ubaldini, E. Giannini, and C. J. van der Beek, Charge puddles in a completely compensated topological insulator, New J. Phys. **18**, 073024 (2016).

[32] S. Essert and K. Richter, Magnetotransport in disordered two-dimensional topological insulators: signatures of charge puddles, 2D Mater. **2**, 024005 (2015).

[33] D. Mallick, S. Mandal, R. Ganesan, and P. S. Anil Kumara, Existence of electron–hole charge puddles and the observation of strong universal conductance fluctuations in a 3D topological insulator, Appl. Phys. Lett. **119**, 013105 (2021).

[34] A. Jash, S. Ghosh, A. Bharathi, and S. S. Banerjee, Exploration of the role of disorder and the behaviour of the surface state in the three-dimensional topological insulator-$Bi_2Se_3$, Bull. Mater. Sci. **45**, 17 (2022).

[35] C. G. Rocha, L. E. F. Foa Torres, and G. Cuniberti, ac transport in graphene-based Fabry-Pérot devices, Phys. Rev. B **81**, 115435 (2010).

[36] L. Arrachea, Green-function approach to transport phenomena in quantum pumps, Phys. Rev. B **72**, 125349 (2005).

[37] D. Cohen, Quantum pumping and dissipation in closed systems, Phys. E **29**, 308 (2005).

[38] D. Cohen, Classical and quantum pumping in closed systems, Solid State Commun. **133**, 583 (2005).

[39] M. Switkes, C. M. Marcus, K. Campman, and A. C. Gossard, An adiabatic quantum electron pump, Science **283**, 1905 (1999).

[40] F. Bourbour, M. Esmaeilzadeh, S. M. Elahi, and L. Eslami, Adiabatic and non-adiabatic quantum charge and spin pumping in zigzag and armchair graphene nanoribbons, J. Appl. Phys. **127**, 164303 (2020).

[41] I. L. Aleiner and A. V. Andreev, Adiabatic Charge Pumping in Almost Open Dots, Phys. Rev. Lett. **81**, 1286 (1998).

[42] D. Kurebayashi and K. Nomura, Voltage-Driven Magnetization Switching and Spin Pumping in Weyl Semimetals, Phys. Rev. Appl. **6**, 044013 (2016).

[43] M. Hori and Y. Ono, Charge Pumping Under Spin Resonance in Si(100) Metal-Oxide-Semiconductor Transistors, Phys. Rev. Appl. **11**, 064064 (2019).

[44] L. E. F. Foa Torres, Mono-parametric quantum charge pumping: Interplay between spatial interference and photon-assisted tunneling, Phys. Rev. B **72**, 245339 (2005).

[45] R. P. Tiwari and M. Blaauboer, Quantum pumping in graphene with a perpendicular magnetic field, Appl. Phys. Lett. **97**, 243112 (2010).

[46] H. Khani, M. Esmaeilzadeh, and F. Kanjouri, Generation of large spin and valley currents in a quantum pump based on molybdenum disulfide, Phys. Chem. Chem. Phys. **19**, 14170 (2017).

[47] K.-R. Jeon, C. Ciccarelli, H. Kurebayashi, J. Wunderlich, L. F. Cohen, S. Komori, J. W. A. Robinson, and M. G. Blamire, Spin-Pumping-Induced Inverse Spin Hall Effect in $Nb/Ni_{80}Fe_{20}$ Bilayers and its Strong Decay Across the Superconducting Transition Temperature, Phys. Rev. Appl. **10**, 014029 (2018).

[48] A. Okada, Y. Takeuchi, K. Furuya, C. Zhang, H. Sato, S. Fukami, and H. Ohno, Spin-Pumping-Free Determination of Spin-Orbit Torque Efficiency from Spin-Torque Ferromagnetic Resonance, Phys. Rev. Appl. **12**, 014040 (2019).

[49] H. Nikoofard, M. Esmaeilzadeh, E. Heidari-Semiromi, and J. T. Sun, Quantum charge and spin pumping in monolayer phosphorene, Phys. Rev. B **102**, 035435 (2020).

[50] M. D. Blumenthal, B. Kaestner, L. Li, S. Giblin, T. J. B. M. Janssen, M. Pepper, D. Anderson, G. Jones and D. A. Ritchie, Gigahertz quantized charge pumping, Nat. Phys. **3**, 343 (2007).

[51] H. Khani, M. Esmaeilzadeh, and F. Kanjouri, Controllable quantum valley pumping with high current in a silicene junction, Nanotechnology **27**, 495202 (2016).

[52] M. Moskalets and M. Buttiker, Magnetic-field symmetry of pump currents of adiabatically driven mesoscopic structures, Phys. Rev. B **72**, 035324 (2005); Time-resolved noise of adiabatic quantum pumps, **75**, 035315 (2007).

[53] P. Samuelsson and M. Büttiker, Dynamic generation of orbital quasiparticle entanglement in mesoscopic conductors, Phys. Rev. B **71**, 245317 (2005).

[54] C. W. J. Beenakker, M. Titov, and B. Trauzettel, Optimal Spin-Entangled Electron-Hole Pair Pump, Phys. Rev. Lett. **94**, 186804 (2005).

[55] M. Jamali, J. S. Lee, J. S. Jeong, F. Mahfouzi, Y. Lv, Z. Zhao, B. K. Nikolic, K. A. Mkhoyan, N. Samarth, and J.-P. Wang, Giant spin pumping and inverse spin Hall effect in the presence of surface and bulk spin-orbit coupling of topological insulator $Bi_2Se_3$, Nano Lett. **15**, 7126 (2015).

[56] M. Alos-Palop, R. P. Tiwari, and M. Blaauboer, Adiabatic quantum pumping through surface states in 3D topological insulators, New J. Phys. **14**, 113003 (2012).

[57] S. Datta, *Electronic Transport in Mesoscopic Systems* (Cambridge University Press, Cambridge, 1995).

[58] Q. Zhang, J.-F. Liu, Z. Lin, and K. S. Chan, Generation of large spin currents in graphene using adiabatic quantum pumping, J. Appl. Phys. **112**, 073701 (2012).

[59] J. An and C. S. Ting, Surface states scattering from a step defect in the topological insulator $Bi_2Te_3$, Phys. Rev. B **86**, 165313 (2012).

[60] H. Li, J. M. Shao, H. B. Zhang, D.-X. Yao, and G. W. Yang, Resonant tunneling in a topological insulator superlattice, J. Appl. Phys. **114**, 093703 (2013).

[61] P. W. Brouwer, Scattering approach to parametric pumping, Phys. Rev. B **58**, R10135(R) (1998).

[62] Q. Zhang, K. S. Chan, and Z. Lin, Spin current generation by adiabatic pumping in monolayer graphene, Appl. Phys. Lett. **98**, 032106 (2011).

[63] Z. B. Siu, M. B. A. Jalil, and S. G. Tan, Topological state transport in topological insulators under the influence of hexagonal warping and exchange coupling to in-plane magnetizations, Sci. Rep. **4**, 5062 (2014).

[64] N. Missault, P. Vasilopoulos, V. Vargiamidis, F. M. Peeters, and B. Van Duppen, Spin-and valley-dependent transport through arrays of ferromagnetic silicene junctions, Phys. Rev. B **92**, 195423 (2015); Spin- and valley-dependent miniband structure and transport in silicene superlattices, **93**, 125425 (2016).

[65] D. Sinha, Spin transport and spin pump in graphene-like materials: effects of tilted Dirac cone, Eur. Phys. J. B **92**, 61 (2019).

[66] Q. Zhang, Z. Lin, and K. S. Chan, Pure spin current generation in monolayer graphene by quantum pumping, J. Phys.: Condens. Matter **24**, 075302 (2012).

[67] S. A. Wolf, D. D. Awschalom, R. A. Buhrman, J. M. Daughton, S. von Molnar, M. L. Roukes, A. Y. Chtchelkanova, and D. M. Treger, Spintronics: A spin-based electronics vision for the future, Science **294**, 1488 (2001).

[68] K.-H. Zhang, Z.-C. Wang, Q.-R. Zheng, and G. Su, Gate-voltage controlled electronic transport through a ferromagnet/normal/ferromagnet junction on the surface of a topological insulator, Phys. Rev. B **86**, 174416 (2012).

[69] C. M. Wang and F. J. Yu, Effects of hexagonal warping on surface transport in topological insulators, Phys. Rev. B **84**, 155440 (2011).

[70] M.-M. Wu, Z.-M. Yu, and H. Pan, The anisotropic effect of hexagonal warping on the transport, Phys. Lett. A **383**, 237 (2019).

[71] X.-Q. Yu, Z.-G. Zhu, and G. Su, Hexagonal warping induced nonlinear planar Nernst effect in nonmagnetic topological insulators, Phys. Rev. B **103**, 035410 (2021).

[72] S.-H. Chen, B. K. Nikolic, and C.-R. Chang, Inverse quantum spin Hall effect generated by spin pumping from precessing magnetization into a graphene-based two-dimensional topological insulator, Phys. Rev. B **81**, 035428 (2010).

[73] A. A. Avetisyan, B. Partoens, and F. M. Peeters, Electric-field control of the band gap and Fermi energy in graphene multilayers by top and back gates, Phys. Rev. B **80**, 195401 (2009).

[74] S. N. H. Sa'don, M. H. Jamaluddin, M. R. Kamarudin, F. Ahmad, Y. Yamada, K. Kamardin, I. H. Idris, and N. Seman, Characterisation of tunable graphene antenna, Int. J. Electron. Commun. **118**, 153170 (2020).

[75] D. T. Comera and D. J. Comer, in *Analog-Signal Electronic Circuits*, 3rd ed., Encyclopedia of Physical Science and Technology (Academic Press, California, 2003), p. 531.

[76] Q. Liu, X.-L. Qi, and S.-C. Zhang, Stationary phase approximation approach to the quasiparticle interference on the surface of a strong topological insulator, Phys. Rev. B **85**, 125314 (2012).

[77] D. A. Khokhlov and R. S. Akzyanov, Quasiparticle interference in doped topological insulators with nematic superconductivity, Phys. E **133**, 114800 (2021).

[78] D. Kim, S. Cho, N. P. Butch, P. Syers, K. Kirshenbaum, S. Adam, J. Paglione, and M. S. Fuhrer, Surface conduction of topological Dirac electrons in bulk insulating $Bi_2Se_3$, Nat. Phys. **8**, 459 (2012).

[79] S. S. Hong, J. J. Cha, D. Kong, and Y. Cui, Ultra-low carrier concentration and surface-dominant transport in

antimony-doped $Bi_2Se_3$ topological insulator nanoribbons, Nat. Commun. **3**, 757 (2012).

[80] N. P. Butch, K. Kirshenbaum, P. Syers, A. B. Sushkov, G. S. Jenkins, H. D. Drew, and J. Paglione, Strong surface scattering in ultrahigh-mobility $Bi_2Se_3$ topological insulator crystals, Phys. Rev. B **81**, 241301(R) (2010).

[81] J. Tian, C. Chang, H. Cao, K. He, X. Ma, Q. Xue, and Y. P. Chen, Quantum and classical magnetoresistance in ambipolar topological insulator transistors with gate-tunable bulk and surface conduction, Sci. Rep. **4**, 4859 (2014).

[82] C.-X. Liu, H. Zhang, B. Yan, X.-L. Qi, T. Frauenheim, X. Dai, Z. Fang, and S.-C. Zhang, Oscillatory crossover from two-dimensional to three-dimensional topological insulators, Phys. Rev. B **81**, 041307(R) (2010).

[83] D.-X. Qu, Y. S. Hor, J. Xiong, R. J. Cava, and N. P. Ong, Quantum Oscillations and Hall Anomaly of Surface States in the Topological Insulator $Bi_2Te_3$, Science **329**, 821 (2010).

[84] J. G. Checkelsky, Y. S. Hor, R. J. Cava, and N. P. Ong, Bulk Band Gap and Surface State Conduction Observed in Voltage-Tuned Crystals of the Topological Insulator $Bi_2Se_3$, Phys. Rev. Lett. **106**, 196801 (2011).

[85] J. Chen, H. J. Qin, F. Yang, J. Liu, T. Guan, F. M. Qu, G. H. Zhang, J. R. Shi, X. C. Xie, C. L. Yang *et al.*, Gate-Voltage Control of Chemical Potential and Weak Antilocalization in $Bi_2Se_3$, Phys. Rev. Lett. **105**, 176602 (2010).

[86] S. Cai, J. Guo, V. A. Sidorov, Y. Zhou, H. Wang, G. Lin, X. Li, Y. Li, K. Yang, A. Li *et al.*, Independence of topological surface state and bulk conductance in three-dimensional topological insulators, npj Quantum Mater. **3**, 62 (2018).

[87] J. Xiong, A. C. Petersen, D. Qua, Y. S. Hor, R. J. Cava, and N. P. Ong, Quantum oscillations in a topological insulator $Bi_2Te_2Se$ with large bulk resistivity (6Ω cm), Phys. E **44**, 917 (2012).

[88] N. Borgwardt, J. Lux, I. Vergara, Zhiwei Wang, A. A. Taskin, Kouji Segawa, P. H. M. van Loosdrecht, Yoichi Ando, A. Rosch, and M. Grüninger, Self-organized charge puddles in a three-dimensional topological material, Phys. Rev. B **93**, 245149 (2016).